

Triplic periodic minimal surface multi-cell interlacing metamaterials to achieve
superior vibration isolation

Mengying Chen¹, Di Lin¹, Hui Qiao, Lei Yang

1. Introduction

Applying lightweight structure to the hull and load-bearing structure can greatly reduce the weight of the hull while meeting the strength requirements, which can not only increase the cargo volume and save fuel costs, but also play the function of vibration isolation^[1]. Ships are subjected to excitation generated by propellers while underway, which causes shaft system vibrations that propagate to the hull^[2]. In order to prevent the vibration generated by the power equipment from being transmitted to the ship's hull, pedestal vibration isolation is one of the more commonly used means of vibration isolation. The base needs to have a certain degree of rigidity, both to carry the weight of the equipment and to meet the requirements of vibration isolation. Vibration isolation can be achieved through the material and structure of the base itself, especially in the case of power equipment where vibration isolators cannot be introduced or installed. Conventional materials such as rubber or springs can reduce vibration to a certain extent, but have low stiffness and cannot be applied.

The porous lattice structure provides excellent mechanical performance and energy absorption, which is widely used in the marine, automotive and aerospace industries.^[3, 4] Over the years, porous structures have predominantly been produced using conventional techniques, including powder metallurgy^[5], combustion synthesis^[6], hot isostatic pressing^[7], vacuum arc remelting, vacuum induction melting and metal injection molding^[8-10]. However, these fabrication methods are inadequate for achieving intricate geometries, precise pore sizes, specific dimensional lengths, and customized mechanical properties. Fortunately, in recent years, rapid advancement in metal-based additive manufacturing (MAM) techniques, such as laser power bed fusion (LPBF) and electron beam melting (EBM), have facilitated the fabrication of highly precise porous metals featuring intricate external geometries and internal structures. Additive manufacturing (AM) technology has proven particularly advantageous in addressing the poor workability of 316L alloys. Presently, through LPBF, 316L alloys can be manufactured into 3D structures with complex geometrical configurations, as opposed to conventional geometries like tubes, rods, wires and sheets.

At present, numerous researchers are investigating Simple Cubic (SC)^[11], Body-Centered Cubic (BCC)^[12, 13], Octahedron structures^[14], Face-Centered Cubic (FCC)^[15], and pyramidal^[16] lattice structure. These structures can be fabricated using additive manufacturing (AM) techniques, which construct parts layer by layer. However, it's important to note that these structures often exhibit uneven and abrupt transitions near joints, resulting in stress concentrations that may lead to premature fractures under load^[17]. Therefore, careful consideration is necessary to address issues related to stress concentration and localized structural failure.

In recent years, researchers have extensively investigated lattice structures based on the triply periodic minimal surface (TPMS). It is also widely found in natural organisms such as butterflies^[18-20]. TPMS surfaces exhibit periodic geometric variations in three independent directions and have a zero mean curvature radius^[21, 22]. These lattice structures not only provide superior manufacturing accuracy but also demonstrate a more uniform stress distribution under load compared to other lattice types, such as body-centered cubic (BCC) and octahedral lattices. The unique characteristics of TPMSs, including their continuous and smooth surfaces with zero curvatures, contribute to these advantages^[23]. The current studies for TPMS have focused on structures such as Gyroid^[24-26], Diamond^[27], IWP^[28], with the most studies for the Gyroid structure. Most of the scholars have studied TPMS by varying the geometrical parameters such as unit cell size and volume fraction. For example, Zhang et al^[29] used Ti6Al4V material to fabricate TPMS lattice structure with certain porosity and pore size to study its mechanical response. The results show that the mechanical properties, deformation mechanism and energy absorption can be changed by linearly changing the sheet thickness and height of the lattice structure.

Other scholars have studied TPMS through innovative ideas such as functional gradient design, multi-morphology(lattice type grading), and multicell interlacing structure design. Yang et al^[30] designed Gyroid structures with gradient structure by LPBF technique which has predictable mechanical response. In particular, modified mathematical equations were utilized to improve the prediction accuracy. The established theory can provide a reference for designing lattice structures with controllable mechanical properties. Oraib et al^[31] comparatively investigated the effects of density gradient, unit cell size gradient, and multi-morphology lattice

structure on the mechanical properties of the structures. The results showed that the mechanical properties were closely related to the compressive loading direction. Finite element analysis showed that the lamellar multi-morphology design has higher elastic properties than the solid multi-morphology design. Jin et al^[24] fabricated from normal Gyroid to octuple interlacing Gyroid Ni-Ti structures by multicell interlacing design using LPBF technique. The superelasticity of the multicell interlacing structures was analyzed by finite element and experiment. The results show that the compression performance of the structure decreases with the increase of the multicell interlacing, but the stress distribution is more uniform. In particular, the proportion of superelastic recoverable strain increases in cyclic compression experiments, demonstrating that the multicell interlacing structures have excellent superelastic properties. Most of the research on TPMS has focused on the mechanical properties. The mechanical properties of TPMS can be improved by changing the structural geometrical parameters and the functional structural design, and the acoustic vibration properties can also be improved. For example, Zhang et al^[32] systematically investigated the effects of volume fraction and unit cell size on the vibration isolation performance of TPMS-IWP-type lattice structures. The results show that changing the geometrical parameters of the lattice structure can modulate the range of low-frequency vibration bandgap. The structure with smaller volume fraction and larger unit cell size has better vibration isolation performance under the premise of guaranteeing the load carrying capacity. Tarcisio et al^[33] investigated the relationship between the bandgap and volume ratio of TPMS. The results show that the width of the bandgap is closely related to the density. The bandgap center frequency is insensitive to the lattice type and is mainly determined by the volume ratio. Lu et al^[34] discussed the relationship between fill rate and bandgap for Primitive and Schoen's F-RD structures. The simulation results show the existence of bandgap in the range of 1.2 kHz-1.7 kHz for both TPMS structures.

Whether in depth or scope, there is a serious problem of lack of research on vibration of TPMS structures. Most of these studies have focused only on comparing different types of TPMS and simply changing geometrical parameters, lacking applied research on the specific performance of TPMS. In addition, only mechanical research exists for the latest multicell structure. In addition, only mechanical research exists for the latest structural design, i.e., multicell interlacing lattice structure, which has

excellent performance in superelasticity, but lacks research on vibration. So it is necessary to study the vibration isolation performance of multicell interlacing lattice structures in ship shafting test and compare the performance of traditional straight rod type BCC and ordinary TPMS. Therefore, in this paper, traditional straight rod type BCC, TPMS-IWP, and interleaved TPMS-IWP lattice structures are fabricated by SLM technology to perform vibration isolation tests on ship shaft system. Some of the conclusions drawn are intended to provide a reference for improving vibration isolation performance through TPMS structural design.

2. Methodologies

2.1 Modeling design

The IWP unit cell is generated by the following functional equations:

$$F(x,y,z,t)=2\cos\left(2\pi\frac{x}{L}\right)\cos\left(2\pi\frac{y}{L}\right)+2\cos\left(2\pi\frac{y}{L}\right)\cos\left(2\pi\frac{z}{L}\right)+2\cos\left(2\pi\frac{z}{L}\right)\cos\left(2\pi\frac{x}{L}\right)-(\cos\left(4\pi\frac{x}{L}\right)+\cos\left(4\pi\frac{y}{L}\right)+\cos\left(4\pi\frac{z}{L}\right))-t \quad (1)$$

in which, the variables a and t control the unit-cell size and volume fraction of the IWP lattice structure, respectively.

The design methodology for multicell interlacing IWP lattice structure is shown in Fig.1. Initially, an IWP lattice structure models with $3 \times 3 \times 3$ unit cells is generated using the TPMS_Scaffold_Generator^[35]. This initial lattice structure is referred to as the Normal IWP lattice structure (NILS). Subsequently, as depicted in Fig. 1(a), two NILSs (specifically, NILS-1 and NILS-2) are prepared before achieving a Double Interlacing IWP Lattice Structure (DIILS).

In the subsequent steps:

1. NILS-2 is translated by a distance of $a/2$ along the X-axis direction, followed by a translational distance of $a/4$ along the Y-axis direction, while NILS-1 remains stationary.
2. The two models are then combined to form a DIILS.

3. Similarly, two DIILSs (namely DIILS-1 and DIILS-2) are planned ahead of attaining a Quadruple Interlacing IWP Lattice Structure (QIILS).
4. DIILS-1 remains stationary, while DIILS-2 is moved by a dimension of $a/8$ along the X-axis direction, followed by a changed dimension of $a/4$ along the Y-axis direction.
5. Finally, both DIILS-1 and DIILS-2 are integrated to form a QIILS.

However, whenever the model is duplicated, the volume fraction (VF) of the resulting lattices must be halved. For instance, both DIILS-1 and DIILS-2 have a VF of 5%, while the original DIILS have a VF of 10%. This adjustment ensures that the overall interlacing structure maintains a fixed VF of 10%. Additionally, the VF and unit-cell size of NILS are set at 10% and 20 mm, respectively. To streamline subsequent investigations, all multicell interlacing models share the same total dimensions of 60 mm \times 60 mm \times 40 mm, a unit-cell size of 20 mm and a VF of 10%. Furthermore, 1 mm thick plates are added to the top and bottom of the designed samples to maintain a flat surface of the lattice structures under compressive loading.

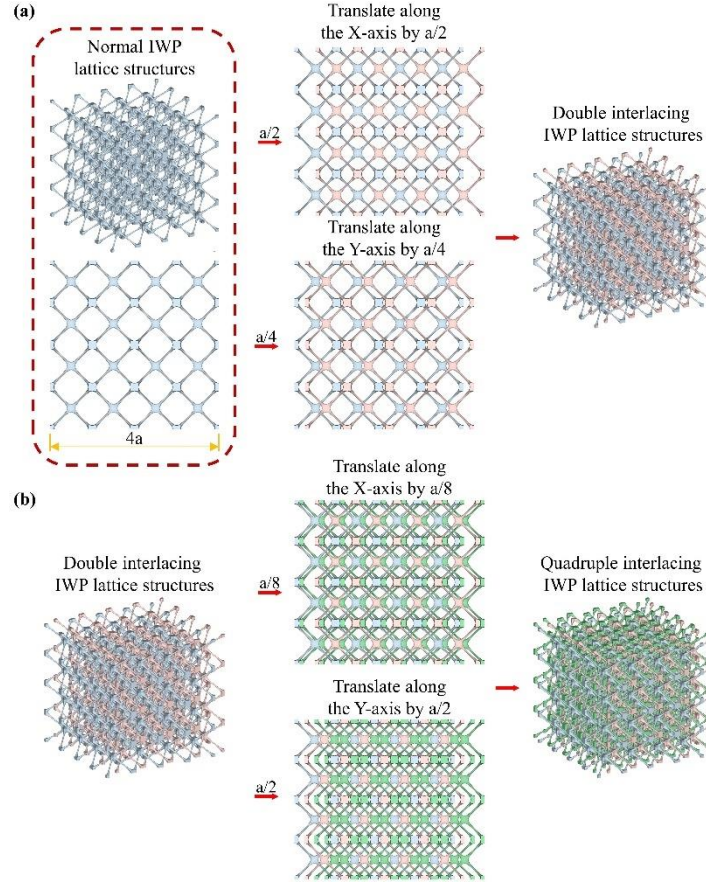


Fig. 1 IWP 多重点阵结构设计：(a) 一重生成二重；(b) 二重生成四重

2.2 Materials and fabrication process

The powder used is 316L, which has a density of 7900 kg/m^3 , an elastic modulus of 210 GPa, and a Poisson's ratio of 0.3. The morphology of 316L powder was observed using a Quanta650 FEG scanning electron microscope (SEM) (FEI, America). As presented in Fig. 2(a), most of the 316L exhibited spherical or near-spherical shapes, and their surfaces appeared smooth. The particle size distribution of 316L powder was determined through a Mastersizer-3000 laser particle size analyzer (Malvern, England). The particle sizes ranged from $19.3 \text{ }\mu\text{m}$ to $53.2 \text{ }\mu\text{m}$, with an average value of $32.1 \text{ }\mu\text{m}$ (Fig. 2 (b)).

In addition, 316L multicell interlacing IWP lattice structures were fabricated by a commercial DiMetal-100H laser powder-bed fusion (L-PBF) machine (Guangzhou

Laseradd Additive Technology Co., Ltd., Guangzhou, China) equipped with a 500-W ytterbium fiber laser. According to the previous experiment ^[32], the printing parameters of LPBF are given in Table 1. To minimize oxidation of 316L powders, the printing process was performed within a printing chamber purged with high-purity argon gas, ensuring the oxygen content remained below 300 ppm. Fig. 2 (c-d) showcases the multicell interlacing samples fabricated by LPBF. These samples exhibit intact overall structures, with each cell being continuous and free from visible cracks or defects.

Table 1 L-PBF parameters

Laser power (w)	scanning velocity (mm/s)	layer thickness (μm)	hatch spacing (μm)	Hatch angle ($^{\circ}$)	volumetric energy density (J/mm^3)
170	900	30	70	90	89.95

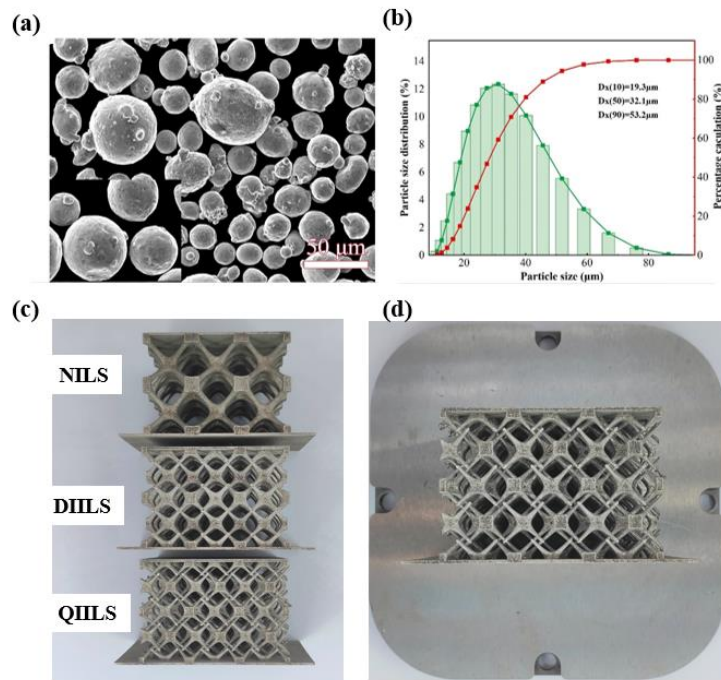


Fig. 2 Powder characterization and samples fabrication (a) Morphology of 316L powder particles; (b) Particle size distribution of 316L powders; (c) Photos of NILS, DIILS and QIILS printed samples; (d) Photo of QIILS fabricated sample.

2.3 Experimental methodologies

2.3.1 Compression test

Considering that the IWP lattice structure fabricated using LPBF exhibits complete symmetry in the X, Y, and Z directions without any noticeable anisotropy, this study primarily investigates the load-bearing and vibrational properties of multicell interlacing IWP lattice structures along the X-axis.

The uniaxial compressive tests on multicell interlacing IWP lattice structures fabricated using LPBF were conducted using an electronic mechanical testing machine (E45.305, China). During the experiments, the bottom plate of the machine was fixed while the top plate was translated at a constant speed of 1/1000 strain rate (0.06 mm/s) of the entire structure downwards according to ISO 13314:2011^[36]. The designed volume fractions of all multicell interlacing samples were 10%. Consequently, the maximum pressure was set to 100 kN for these samples to achieve adequate deformation. Detailed deformation behavior of these IWP lattice structures was meticulously recorded using a video camera during the compressive process.

Based on the stress-strain curves, we can determine the Young's modulus E_{cel} , energy absorption E , onset strain for densification ϵ_{cd} , maximum yield stress σ_s , energy absorption per unit volume W_v for the fabricated samples using LPBF. Additionally, the plateau stress, σ_{pl} corresponds to the average stress within the strain range of 20% to 50%.

The energy absorption can be calculated by integrating the area under the load-displacement curve using the following expression:

$$E(s) = \int_0^s F(s) ds \quad (2)$$

in which $F(s)$ represents the load at a specific displacement s .

Specific energy absorption refers to the energy absorbed per unit mass:

$$SEA(s) = \frac{E}{m} = \frac{\int_0^s F(s)ds}{m} \quad (3)$$

The unit volume energy absorption can be determined by integrating the compressive stress-strain curve, defined as:

$$W_v = \int_0^\varepsilon \sigma(\varepsilon) d\varepsilon \quad (4)$$

Where W_v refers to the energy absorption per unit volume (MJ/m³), ε represents the strain and σ is the compressive stress.

Energy absorption efficiency is defined as the ration of energy absorbed at a certain strain to the corresponding strain:

$$\eta(\varepsilon) = \frac{1}{\sigma(\varepsilon)} \int_0^\varepsilon \sigma(\varepsilon) d\varepsilon \quad (5)$$

The starting stress of densification occurs at the strain where the energy absorption efficiency reaches its maximum value, indicated by a zero slope in the energy absorption efficiency curve:

$$\left. \frac{d\eta(\varepsilon)}{d\varepsilon} \right|_{\varepsilon=\varepsilon_{cd}} = 0 \quad (6)$$

2.3.2 Vibration response test

For an IWP lattice structure, a simple harmonic can be applied at its base and the isolation performance can be evaluated by measuring the input response on the excitation side and the output response on the opposite side. Vibration isolation performance is typically expressed in terms of displacement transfer rate, force transfer rate and acceleration transfer rate. In this study, we measured the acceleration response, as shown in Fig. 3(a), to determine the input response A_0 and output response A_1 of the structure. Here, A_1 represents the acceleration amplitude at the vibration response point, while A_0 represents the acceleration amplitude at the excitation or source end. The vibration level difference VLD, was defined using the following equation:

$$VLD = 20 * \log_{10}(A_1/A_0) \quad (7)$$

Therefore, when $A_1/A_0 < 1$, it means that the response at the output is less than the response at the input, and the structure will produce vibration isolation when $VLD < 0$.

The damping ratio of both structures were also tested for frequency response analysis. The structural damping ratio ζ is defined using the following expression:

$$\zeta = \frac{1}{2} \frac{f_{\max} - f_{\min}}{f_0} \quad (8)$$

where, f_0 represents the resonant frequency, f_{\min} and f_{\max} , as illustrated in Fig. 3 (b), are the frequencies corresponding to half-power amplitude $\frac{Y_{\max}}{\sqrt{2}}$, respectively.

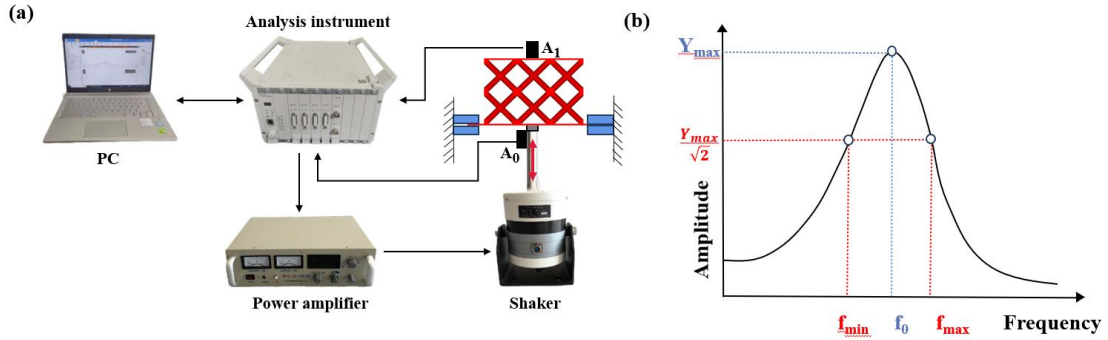


Fig. 3 Schematic diagram of the experimental: (a) Dynamic characterization through a vibration test; (b) The Half-power bandwidth method 图重新画

To investigate the vibration isolation performance of the multicell interlacing IWP lattice structures, dynamic vibration tests were conducted using experimental devices as depicted in Fig. 3. The sample's base was secured with a set of fixtures serving as boundary conditions. A sinusoidal excitation signal ranging from 0 to 5000 Hz was input into the dynamic signal analyzer, which transmitted it to the exciter (HEV-50) via the power amplifier (HEAS-50). The excitation was then applied to the sample's base through the force transducer (3A105). The acceleration signal was captured by the acceleration sensor (1A116E) and sent to the PC for further processing. Finally, we calculated the vibration level difference VLD based on the equation (7).

2.3.3 Shaft system vibration test

The designed and installed shaft system models and shaft system object are depicted in Fig.4.

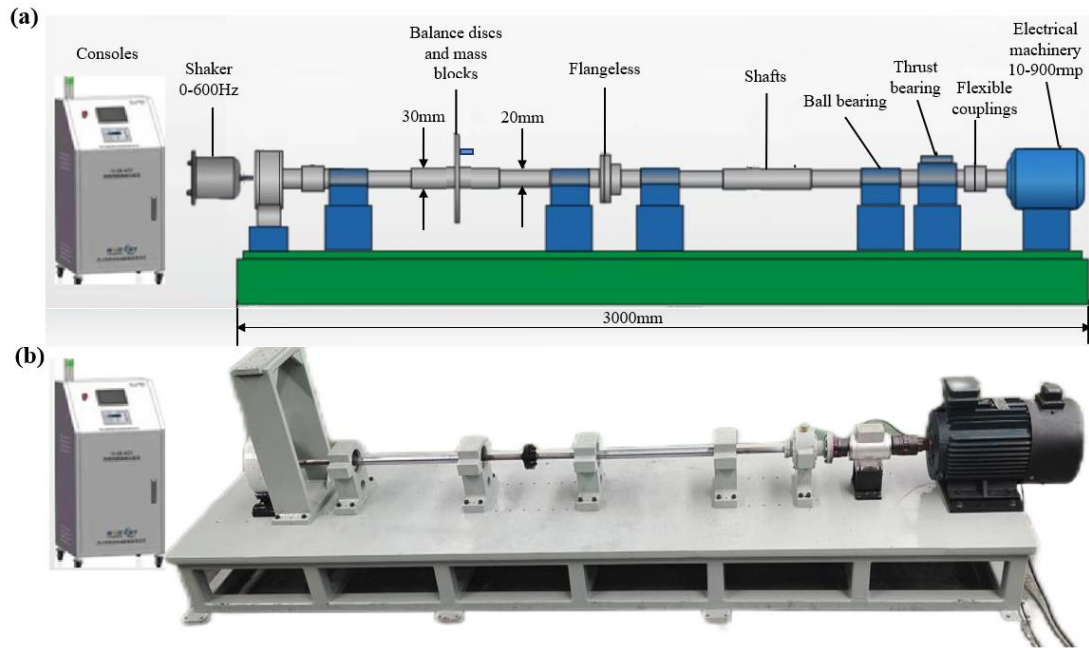


Fig. 4 Shaft propulsion system and consoles: (a) Shaft system model; (b) Shaft system object

Three kinds of multicell interlacing IWP lattice structure isolation base including NILS, DIILS, and QIILS base were utilized to analyze the vibration isolation effects. In addition, we included a set of solid structure bases as control group. The lattice structure isolation bases are designed as shown in Fig. 5(a) and (b), the solid structure bases are depicted in Fig. 5(b), the acceleration sensor arrangement is shown in Fig. 5(d).

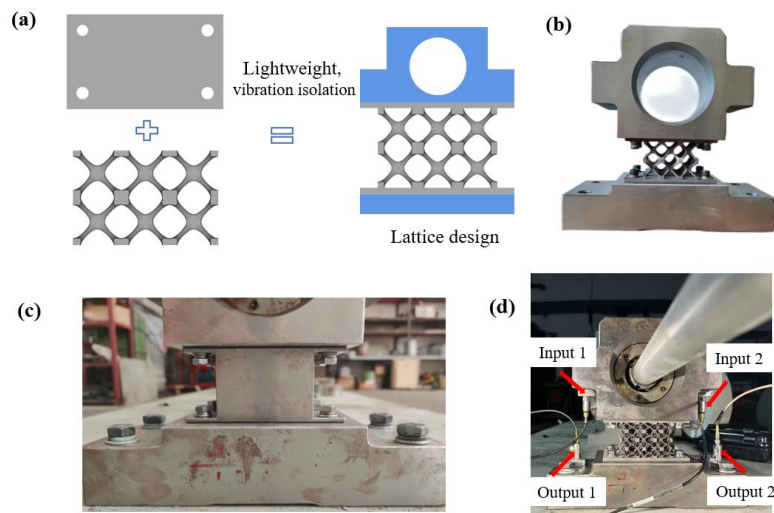


Fig. 5 Lightweight lattice structure shaft system vibration isolation base design: (a)

Lattice structure vibration isolation base design model drawing; (b) Physical drawing of lattice structure vibration isolation base; (c) Physical drawing of solid structure vibration isolation base; (d) Acceleration sensor layout schematic

As shown in Fig. 6, we subjected the stern to longitudinal excitations using vibrators within the frequency range of 0 to 600 Hz. To ensure the experiment's accuracy, four acceleration sensors (including two input-response and two output-response sensors) were securely affixed to the upper and lower ends of the lattice structure using magnetic mounts. This arrangement enabled us to capture the comprehensive vibration response of the base.

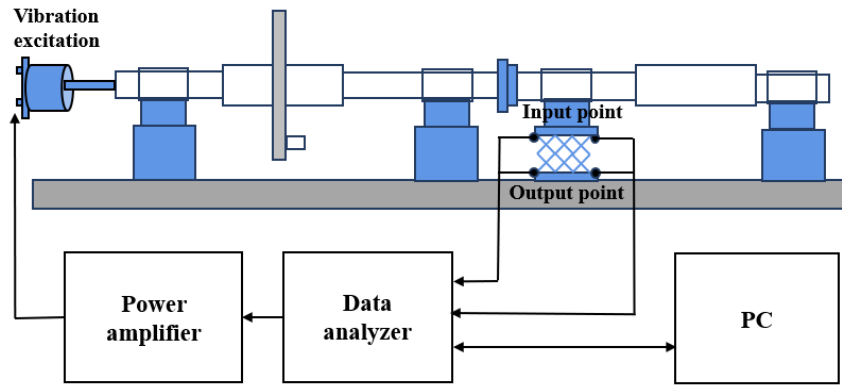


Fig. 6 Shaft system vibration test schematic diagram

3. Results and discussion

3.1 Mechanical properties analysis

Compression tests were performed on 10% volume fraction multi-cell interlacing structures, each of which was compressed twice. The stress-strain curves are shown in Fig. 7. It can be seen that the two compression curves overlap well, especially in the linear elastic phase and at the onset of plateau stress phase (corresponding to strains of 5%-15%). For the NILS, the two curves differed near 25% and 35% strain with significant fluctuations, mainly due to the possibility of some defects in the SLM fabricated structure, and it was found that some of the rods of the structure fractured during the compression process. In addition, the stress-strain curves of the NILS exhibit significant fluctuations, but those of the DIILS and QIILS are more smooth, which is attributed to the combination of multi-cell interlacing structural approach.

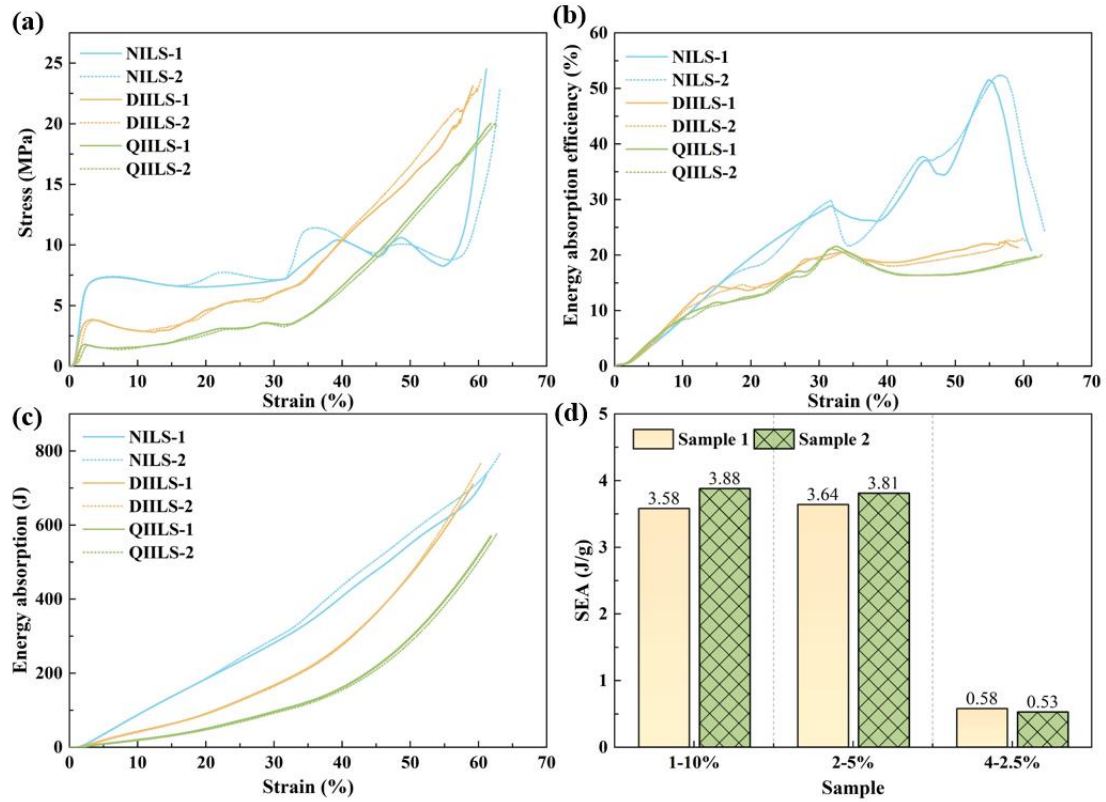


Fig. 7 Mechanical properties of multi-cell interlacing structures: (a) Stress-strain curve; (b) the energy absorption efficiency-strain curves; (c) The total energy absorption-strain curves; (d) The energy absorption per unit quality

Based on the stress-strain curves, the main mechanical properties of the multi-cell interlacing structures were calculated, as shown in Table 2. The average Young's moduli of the three structures were 498 MPa, 302 MPa and 162 MPa, respectively. The Young's modulus decreased by a factor of 0.39 for the DIILS compared to the NILS, and by a factor of 0.46 for the QIILS compared to the DIILS. It is shown that the larger the number of unit interlacing, the more obvious the decrease of mechanical properties. The main reason is that with the increase of the number of unit interlacing, the structural rods will become thinner and thinner, resulting in more and more defects, which also has a big impact on the load-bearing performance of the structure. The yield strength decreases by a factor of 0.46 and 0.5, respectively, with the increase in the number of unit interlacing, which is almost a waist-deep decrease. It can also be noticed from the table that comparing NILS and QIILS, the energy uptake is almost unchanged, but the energy uptake of QIILS decreases abruptly, which is mainly related to its densification

initiation stage. The onset of densification stage of NILS and DIILS is between 55% and 58%, but due to the higher number of interleaved QIILS units, the number of structural singletons is four times as many as that of NILS, and therefore the internal nodes are also four times as many as that of NILS. The nodes occupy almost most of its internal pores, so the beginning of the densification phase occurs near 32% strain during compressive deformation.

Table 2 Mechanical properties of multi-unit interlacing structures

sample	E_{cel} (MPa)	ϵ_{cd} (%)	σ_s (MPa)	W_v (MJ/m ³)	σ_{pl} (MPa)
1-10%-1	485±0.81	55.09	6.18	427.46	6.75
1-10%-2	511±0.15	56.60	6.27	462.97	7.14
2-10%-1	304±0.56	57.35	3.42	453.91	4.35
2-10%-2	300±0.48	57.69	3.28	473.84	4.27
4-10%-1	176±0.27	32.61	1.72	75.93	2.62
4-10%-2	148±0.23	31.79	1.65	69.79	2.52

The energy absorption capacity of the multi-cell interlacing structures is shown in Fig. 7(b). The energy absorption efficiency curves of the multi-cell interlacing structures gradually increase in the range of linear elasticity at the beginning. However, after 10% strain, the energy absorption efficiency appears to be different, especially the energy absorption efficiency of NILS is much larger than that of DIILS and QIILS. The maximum energy absorption efficiency of NILS reaches more than 50%, which is two and a half times higher than that of DIILS and QIILS. It is shown that the energy absorption efficiency of the lattice structure is severely reduced as the number of cell insertions increases manifold, which is mainly related to the excessively fine rod diameter and the densification onset. The energy absorption per unit mass of the multi-cell interlacing structures is shown in Fig. 7(d). The total energy absorption of QIILS is less due to the lower load carrying capacity and smaller densification onset strain of QIILS. The energy absorption per unit mass is also only about 0.5 J/g, which is much less than that of NILS and DIILS. In addition, QIILS has a larger surface area and more metal powder adheres to the surface of the structure, which also increases the overall mass of the structure resulting in lower energy absorption per unit mass.

3.2 Vibration Performance Analysis

A sinusoidal sweep is performed on the multi-cell interlacing structure and the Fig. 8 shows the frequency response curves of the three multi-cell interlacing structure with good overlap. The first intrinsic frequencies of NILS, DIILS and QIILS are in the

vicinity of 2200 Hz, 1998 Hz and 1583 Hz due to the increase in the number of weights, the structural rod diameter becomes thinner and the stiffness decreases gradually, so that the first-order intrinsic frequency decreases gradually.

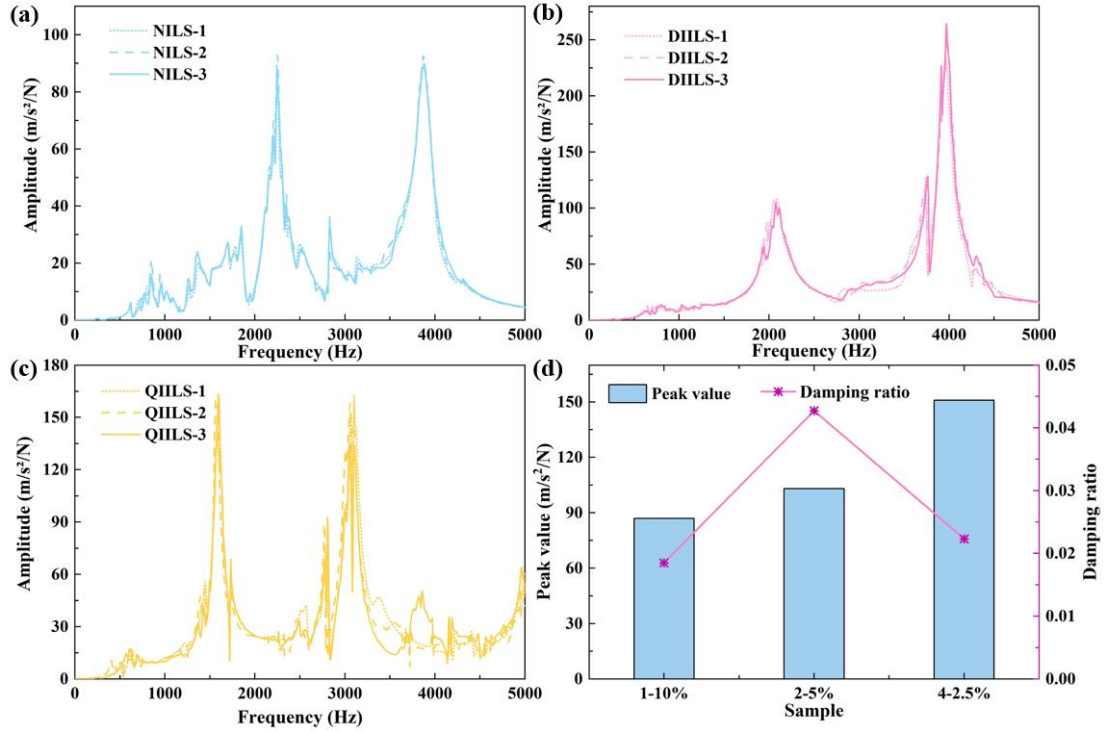


Fig. 8 Frequency response of 10% multi-cell interlacing structures: (a), (b) and (c) Frequency response of NLS, DIILS and QIILS; (d) Average resonance peaks and damping ratios of multi-cell interlacing structures

Based on the frequency response curves and the damping ratio formula, the damping ratio of the multi-cell interlacing structures was calculated. Figure 8(d) shows the average peak magnitude and damping ratio of the multi-cell interlacing structures at resonance. There is no definite relationship between the damping ratio and the number of multi-cell interlacing structures, and the inverse relationship between the damping ratio and the peak value is not satisfied. This is different from the uniform and gradient lattice structures that exhibit the regularity of increasing damping ratio and decreasing peak value^[32]. It indicates that for multi-cell interlacing structures, as the number of cell interlacing increases manifold, there is an effect on the structural damping ratio and resonance peak.

Table 3 The resonance amplitude and damping ratio of multi-cell interlacing structures

sample	tests	resonance amplitude	f_0	f_{\min}	f_{\max}	damping ratio
1-10%	1	81.703	2250	2193.75	2275	0.0181
	2	92.772	2250	2200	2281.25	0.0181
	3	86.405	2250	2193.75	2281.25	0.0194
2-10%	1	104.464	2075	2018.75	2175	0.0377
	2	102.171	2075	1993.75	2187.5	0.0467
	3	102.63	2068.75	1981.25	2162.5	0.0438
3-10%	1	153.451	1593.75	1550	1625	0.0235
	2	148.494	1575	1543.75	1606.25	0.0198
	3	150.638	1581.25	1556.25	1631.25	0.0237

The vibration level difference curves of the multi-cell interlacing structure are shown in Fig. 9. Comparing the vibration isolation performance of NILS, DIILS and QIILS, within 0-600 Hz, the frequency band with the best vibration isolation effect of NILS is between 250-450 Hz, and the amplitude of the largest vibration level drop can reach 17.5 dB. The level drop of both DIILS and QIILS is basically above 5 dB, with the maximum vibration level difference between 17.5 dB and 20 dB. As the number of cell interlacing increases, the stiffness becomes smaller, and the vibration isolation band gap gradually approaches the low frequency.

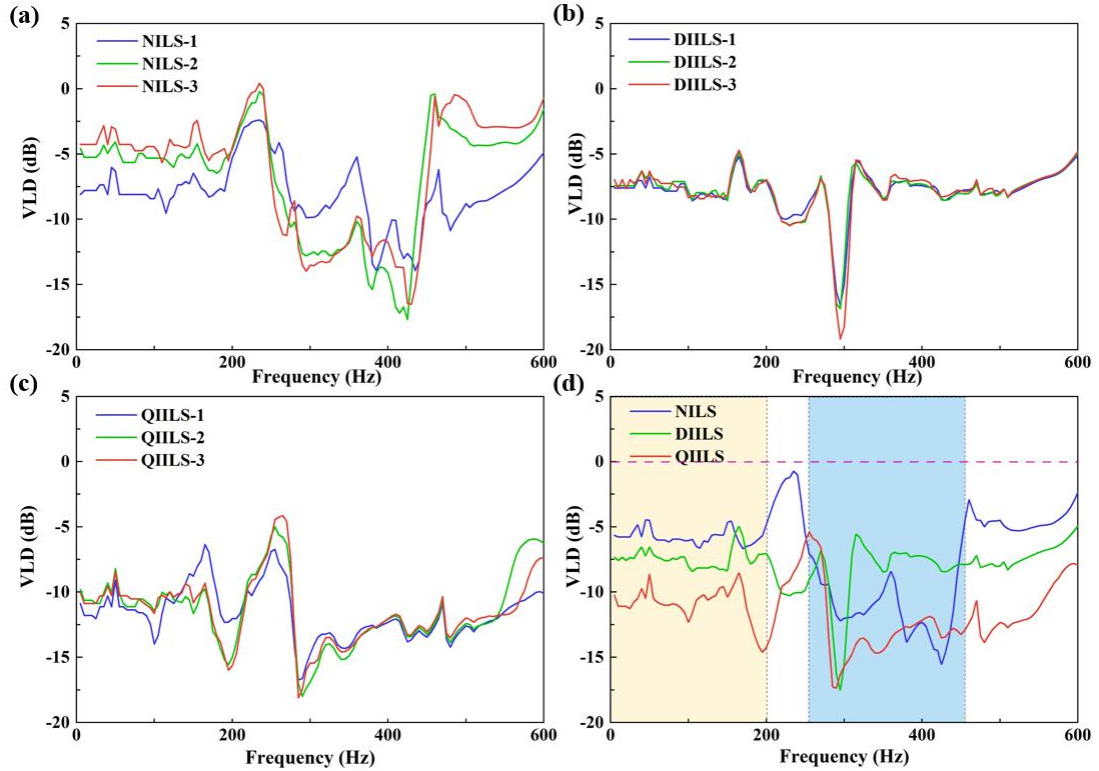


Fig. 9 Multi-cell interlacing structure vibration level difference: (a), (b) and (c) NILS,

DIILS and QIILS; (d) Average vibration level difference

Within 0-600 Hz, the average vibration isolation effect is shown in Fig. 9(d). Comparing the vibration isolation effects of NILS, DIILS and QIILS, it is clearly observed that the maximum vibration level drop of QIILS in the range of 0-200 Hz can reach more than 10 dB, which indicates that the multi-cell interlacing design can further improve the vibration isolation effect of the lattice structure.

3.3 Performance analysis of vibration isolation base for lattice structure

In order to better verify the vibration isolation effect of the designed lattice structure vibration isolation base on the shaft system, four kinds of structures were designed and the ship propulsion shaft system was built. Vibration tests were conducted by applying transverse and longitudinal vibration excitations at different rotational speeds to evaluate the vibration isolation effect of the propulsion shaft system lattice structure base.

In order to analyze the vibration isolation effect of the lattice structure vibration isolation base in the shaft system, the vibration response results are discussed from three working conditions. The three working conditions are: i. Longitudinal excitation is applied at the stern to simulate external excitation of the stationary system when the shaft system is stopped. ii. Loaded with balancing discs and unbalanced mass blocks to simulate the rotational transverse excitation generated by the shaft at different rotational speeds. iii. longitudinal excitation of the transom and transverse excitation resulting from the rotation of the mass block.

3.3.1 Characterization of shaft system vibration under longitudinal excitation of the stern

According to the response results in Fig. 10, the four structures produce large resonance peaks near 100 Hz and 300 Hz after the shaker input 0-600 Hz excitation. As shown in Fig. 10, the input and output vibration response curves of the solid structure base are almost identical, which means that the solid structure does not provide vibration isolation. The vibration isolation effect is obvious only between 350-550Hz. For BCC lattice structure, it has vibration isolation effect within 0-100Hz, and its vibration isolation effect is more obvious after 300Hz, especially near 400Hz. From

Fig. 10(c) and (d), it can be seen that the vibration response curves of NILS and QIILS have a similar trend, which produces an obvious vibration attenuation near 300 Hz. Both structures are TPMS structures, indicating that the TPMS-designed lattice vibration isolation base has better vibration isolation effect than the traditional straight rod BCC structure.

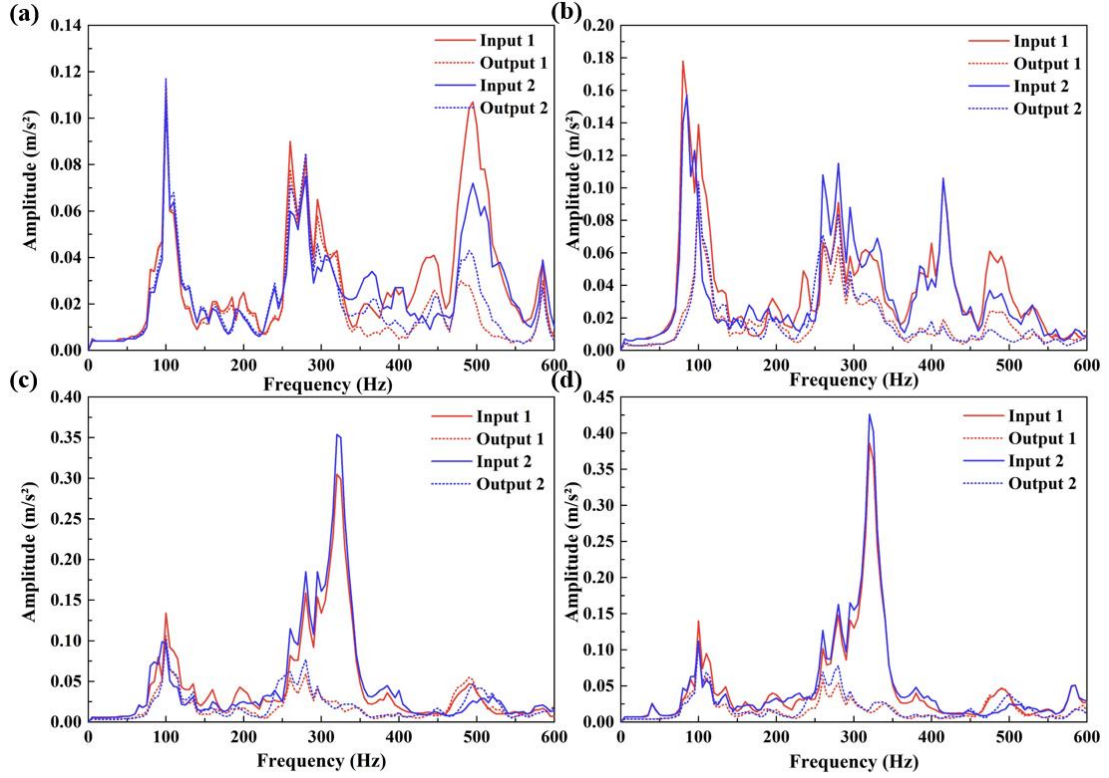


Fig. 10 Vibration response of the axial base with different structures during longitudinal excitation of the stern: (a) Solid structure; (b) BCC; (c) NILS; (d) QIILS

In order to observe the vibration isolation effect of the four structures more intuitively, the VLD calculated using Eq. (2-7) are shown in Fig. 11. From Fig. 11(a), it can be seen that within 300 Hz, the level drop curves are all around 0 dB, representing that the solid structure has no vibration isolation effect. For the BCC lattice structure, a wide isolation bandgap is generated around 80 Hz, 235 Hz, and 400 Hz with a maximum VLD of 18.8 dB. For NILS and QIILS, on the other hand, a large isolation bandgap is generated near 325 Hz with maximum VLD of 26.4 dB and 29.5 dB, respectively. It is noteworthy that comparing NILS and QIILS, QIILS produces 15 dB of vibration isolation at low frequency 40 Hz (as shown by the arrows in Fig. 11(d)), which indicates that the multi-cell interlacing design has better low-frequency vibration

isolation. It is feasible to control low-frequency vibration through multi-cell interlacing design.

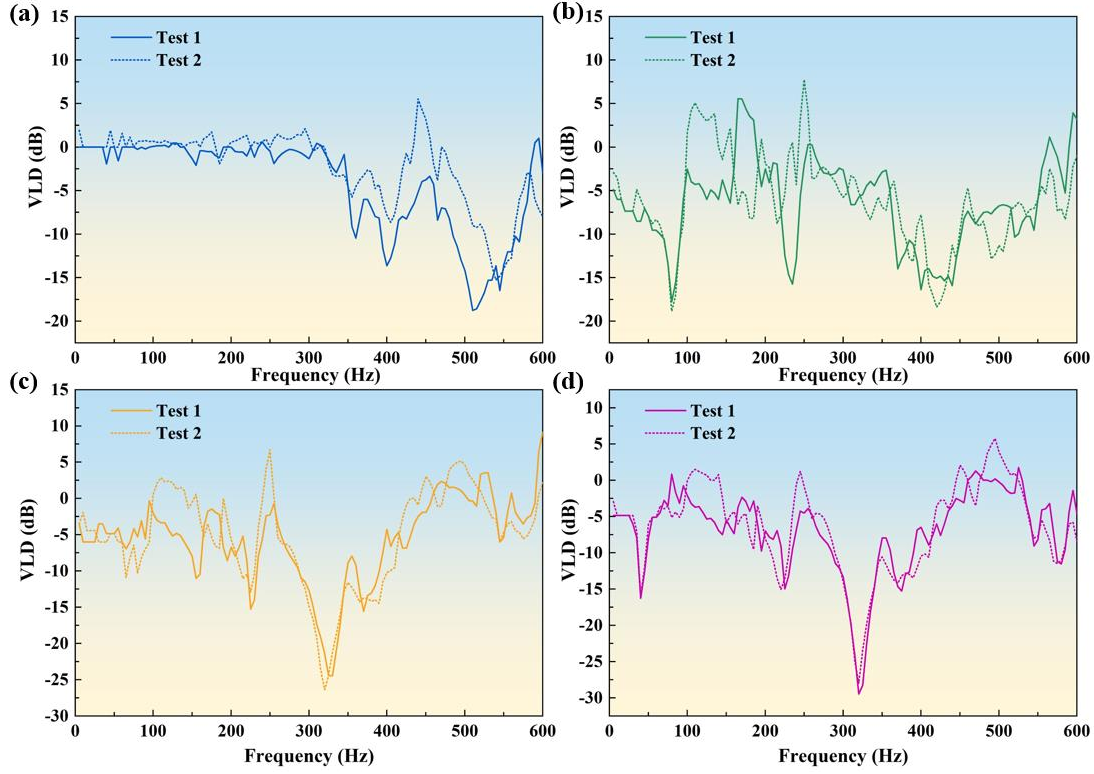


Fig. 11 VLD of different structural shafting bases during longitudinal excitation of the stern: (a) Solid structure; (b) BCC; (c) NILS; (d) QIILS

3.3.2 Characterization of shaft system vibration under lateral excitation of rotational unbalance force

In order to analyze the vibration isolation effect of the shaft at different rotational speeds of the lattice structures bearing vibration isolation base, the vibration responses of the four structures were tested at 200 rpm, 400 rpm, and 600 rpm rotational speeds, respectively, under the second operating condition.

The vibration responses of the solid, BCC, NILS and QIILS are shown in Figs. 12-15. Fig. 12 shows that the solid structure has almost no vibration isolation effect at 0-300 Hz for different rotational speeds, while for BCC, NILS and QIILS, the TPMS-designed base exhibits good vibration isolation effect. Among them, NILS and QIILS have the largest vibration level drop, which is consistent with the vibration isolation performance in the first working condition. In addition, with the change of rotational

speed, the trends of the vibration level difference curves at the three rotational speeds show a high degree of similarity, and the amplitude of the vibration level difference gradually increases, especially for QIILS, where the increase is the most pronounced.

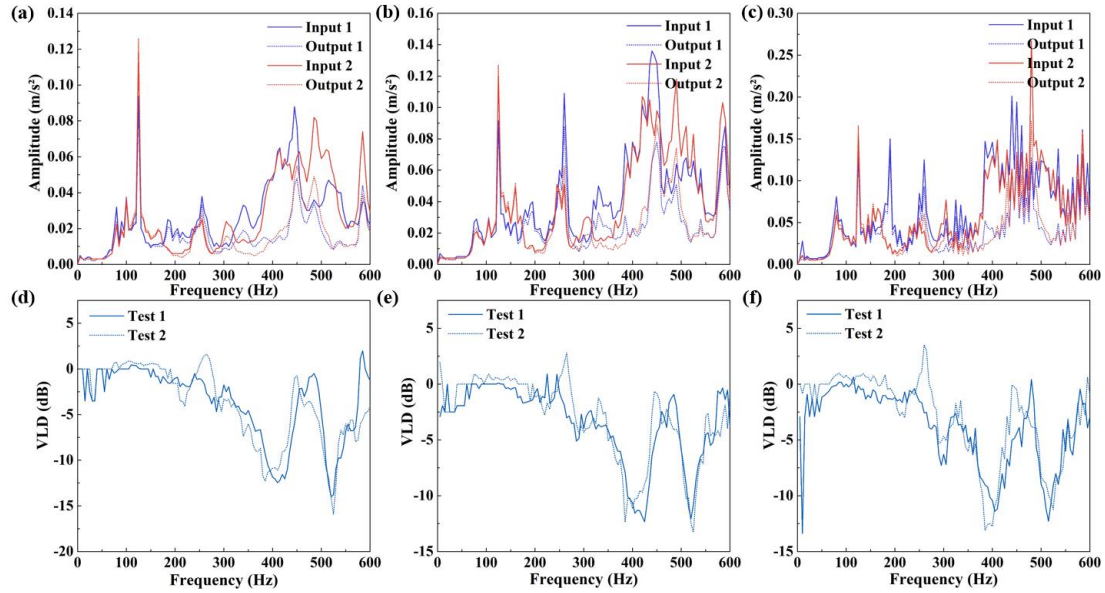


Fig. 12 Vibration response of the solid structure at different rotational speeds: (a), (b) and (c) Acceleration input and output responses at 200 rpm, 400 rpm, and 600 rpm; (d), (e) and (f) VLD at 200 rpm, 400 rpm, and 600 rpm.

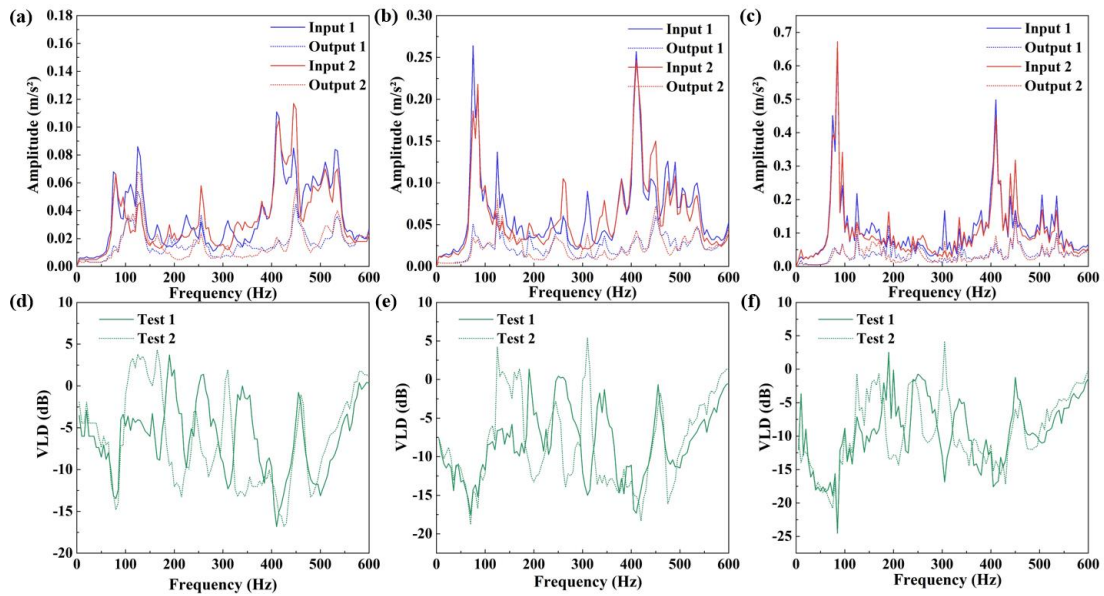


Fig. 13 Vibration response of BCC at different speeds: (a), (b) and (c) Acceleration input and output responses at 200 rpm, 400 rpm, and 600 rpm; (d), (e) and (f) VLD at 200 rpm, 400 rpm, and 600 rpm.

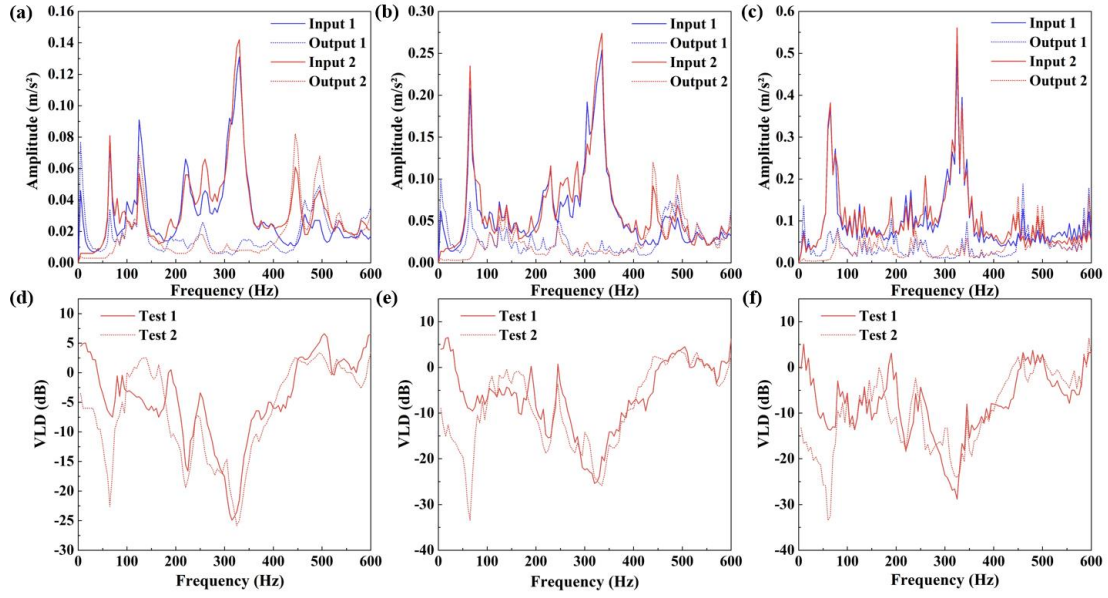


Fig. 14 Vibration response of NILS at different speeds: (a), (b) and (c) Acceleration input and output responses at 200 rpm, 400 rpm, and 600 rpm; (d), (e) and (f) VLD at 200 rpm, 400 rpm, and 600 rpm

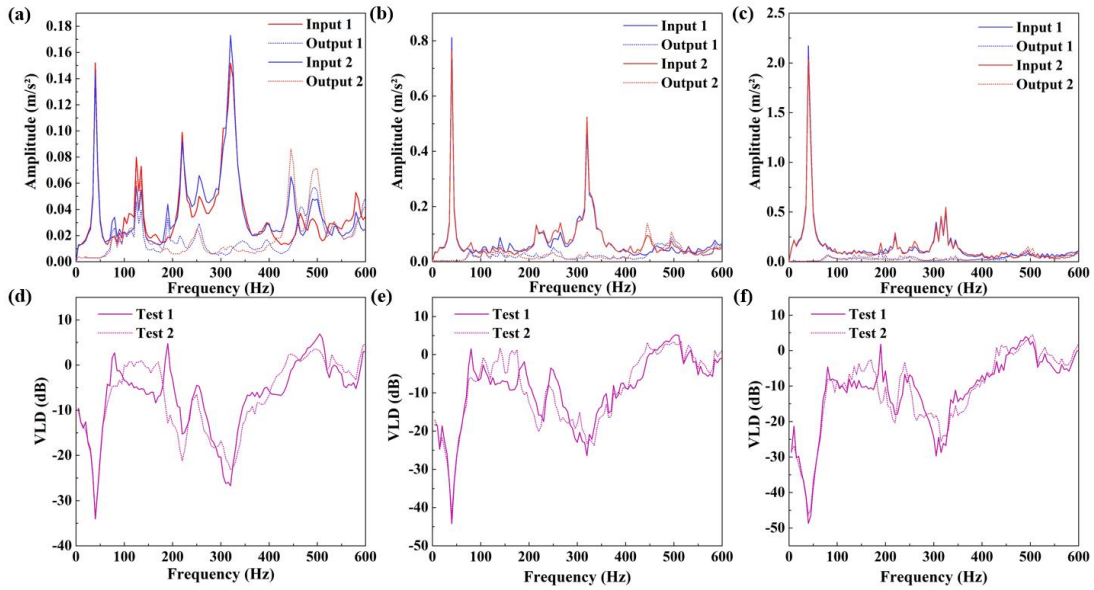


Fig. 15 Vibration response of QILS at different speeds: (a), (b) and (c) Acceleration input and output responses at 200 rpm, 400 rpm, and 600 rpm; (d), (e) and (f) VLD at 200 rpm, 400 rpm, and 600 rpm

Observing the vibration response curves in Figs. 12-15 (a), (b) and (c), the vibration response curves of the four structures gradually go from smooth to jagged as the rotational speed rises from 200 rpm to 600 rpm, which is mainly due to the

equilibrium disk as well as the unbalanced mass block mounted on the shaft system. Taking 600rpm speed as an example, the vibration frequency of the unbalance force generated by the shaft system during rotation is $f=600\div 60=10\text{Hz}$, so a higher vibration response is generated every 10Hz. While at low rotational speeds, the excitation force generated by the unbalance block is relatively small and the vibration response of the shaft system is also small. As the rotational speed increases, the input exhibits higher vibration peaks.

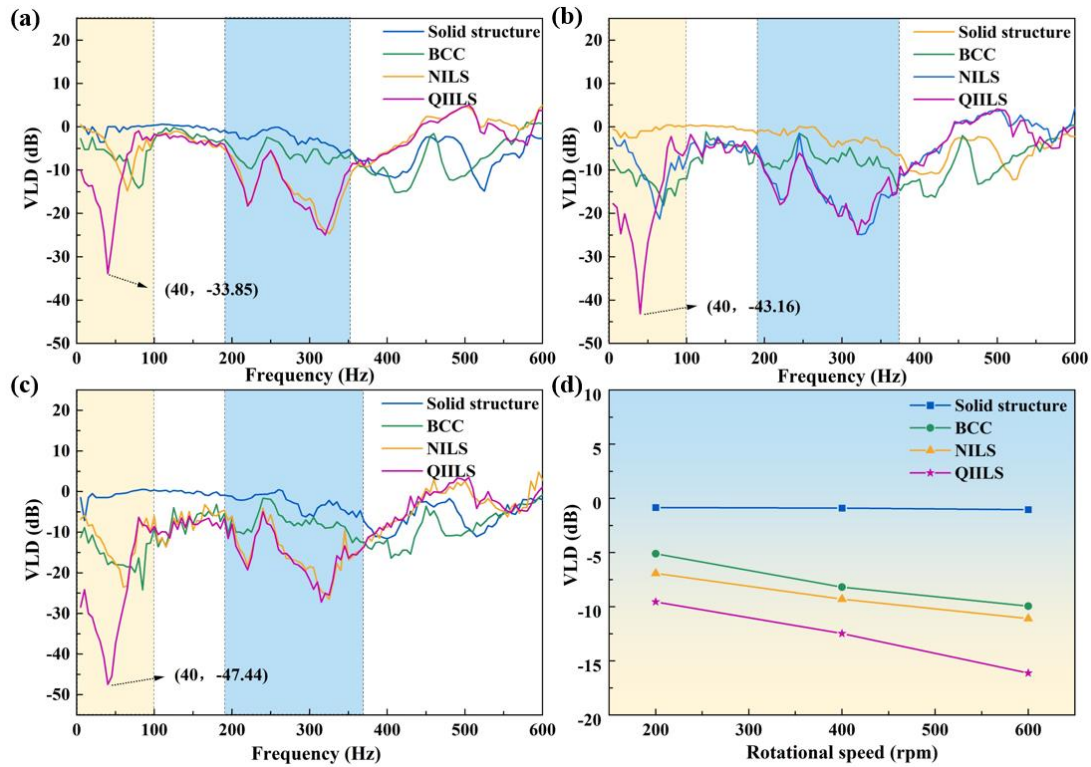


Fig. 16 VLD of different structures at different rotational speeds: (a), (b) and (c) VLD at 200rpm, 400rpm and 600 rpm; (d) average VLD from 0-300 Hz

In order to compare the vibration isolation effect of the four structures more clearly, the average vibration response of the two outputs and inputs are averaged and then plotted as the average vibration level difference curve. Figure 16 shows the average vibration response of different structures at different speeds. As shown in Figs. 16(a), (b) and (c), the solid structure shows almost no vibration isolation at different rotational speeds. In contrast, BCC, NILS and QIILS show good vibration isolation performance, producing two wide vibration isolation band gaps between 0-100 Hz and 200-400 Hz. It can also be observed that between the second vibration isolation bandgap, the

vibration level difference between NILS and QIILS is larger than that of BCC, indicating that the vibration isolation of the TPMS lattice structure is more effective as compared to the conventional straight rod type point structure. For NILS and QIILS, both consist of IWP unit cells, the difference being that QIILS consists of four NILS with smaller volume fractions and therefore has less stiffness. At low frequencies, the QIILS exhibits significant vibration isolation, with the maximum vibration level difference increasing from 33.85dB to 47.44dB as the speed increases from 200rpm to 600rpm.

Under the third operating condition, in order to observe the effect of different rotational speed magnitudes on the vibration isolation, the average vibration level drop for the four structures from 0-300 Hz was calculated, as shown in Fig. 16(d). It is obvious from the figure that the solid structure has almost no vibration isolation effect, and for the other three lattice structures, the higher the rotational speed, the higher the average vibration level drop. For the four structures, the vibration isolation effects are, from best to worst: QIILS > NILS > BCC > solid structure. The main reason is that the lattice structure serves as the middle part of the base, connecting the upper and lower parts of the base. Compared to the solid structure, the lattice structure has less stiffness. The stiffness of the whole base structure is out of balance and the impedance mismatch is more serious^[37]. In contrast, NILS and QIILS, which consist of IWP unit cells, exhibit better vibration isolation performance than the BCC structure in the axial vibration isolation test due to the change in rod gradient.

3.3.3 Characterization of shaft system vibration under longitudinal and transverse excitation

In order to analyze the vibration isolation effect of the lattice structure axial vibration isolation base under the combined effect of the longitudinal excitation of the stern and the transverse excitation of the rotational imbalance force generated by different rotational speeds, the vibration responses of the four structures were tested at 200 rpm, 400 rpm, and 600 rpm, respectively, under the third operating condition. The vibration responses of the solid structure, BCC, NILS and QIILS are shown in Figs. 17-20, respectively.

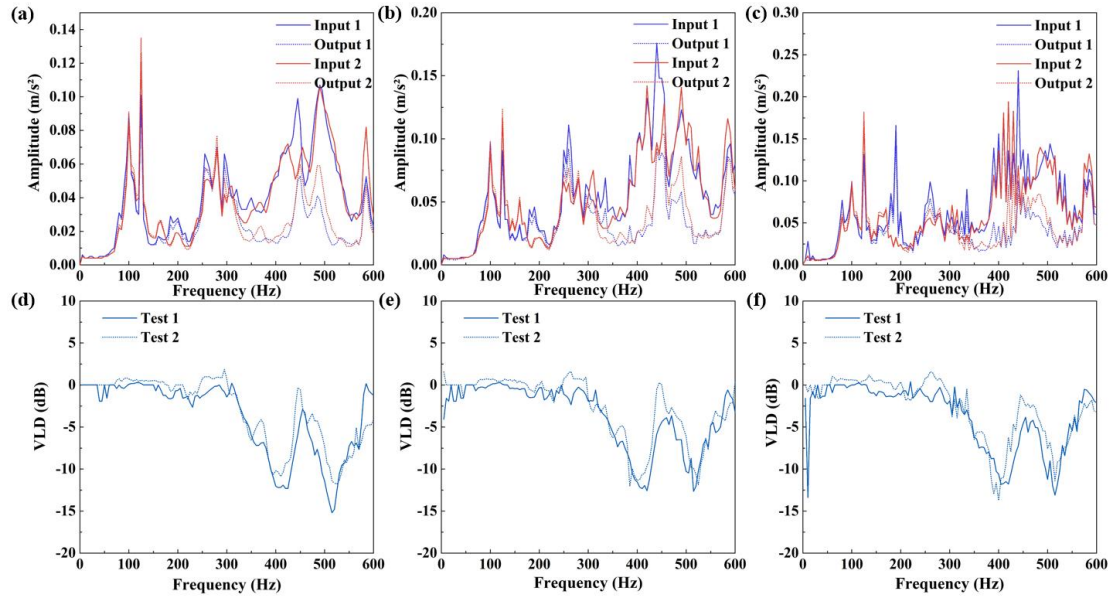


Fig. 17 Vibration response of solid structure under the combined effect of rotating transverse excitation and stern longitudinal excitation: (a), (b) and (c) Acceleration input and output responses at speeds of 200rpm, 400rpm and 600 rpm; (d), (e) and (f) VLD at speeds of 200rpm, 400rpm and 600 rpm

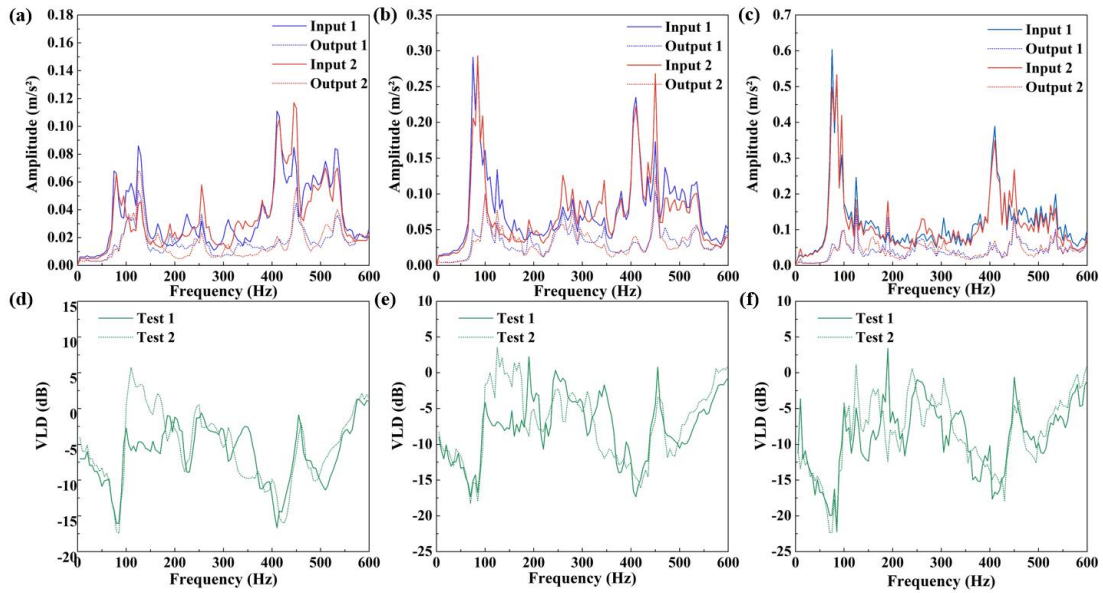


Fig. 18 Vibration response of BCC under the combined effect of rotating transverse excitation and stern longitudinal excitation: (a), (b) and (c) Acceleration input and output responses at speeds of 200rpm, 400rpm and 600 rpm; (d), (e) and (f) VLD at speeds of 200rpm, 400rpm and 600rpm

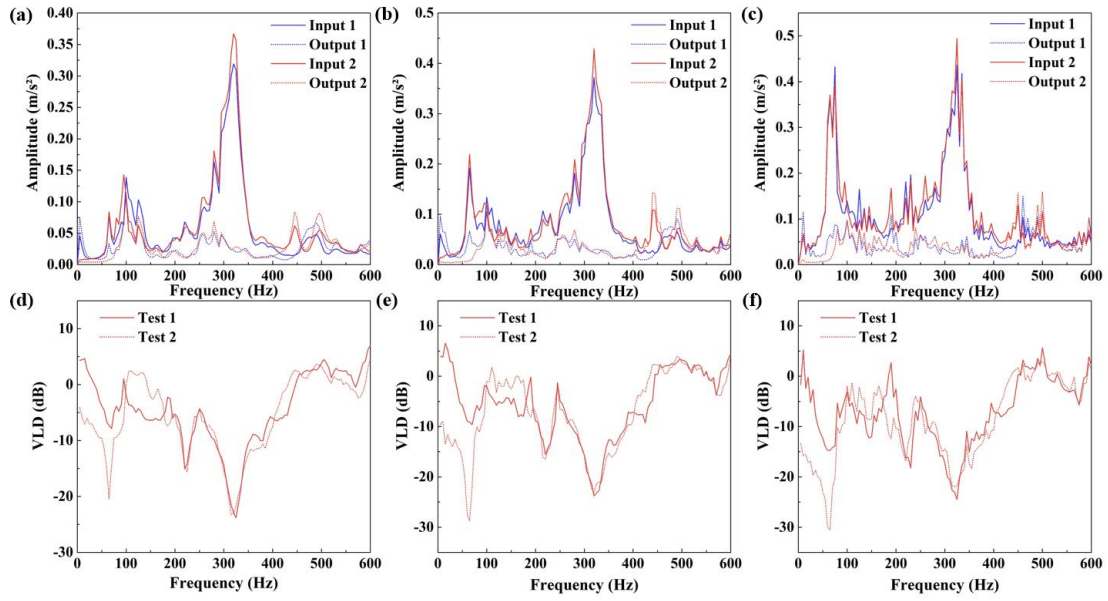


Fig. 19 Vibration response of NILS under the combined effect of rotating transverse excitation and stern longitudinal excitation: (a), (b) and (c) Acceleration input and output responses at speeds of 200rpm, 400rpm and 600 rpm; (d), (e) and (f) VLD at speeds of 200rpm, 400rpm and 600 rpm

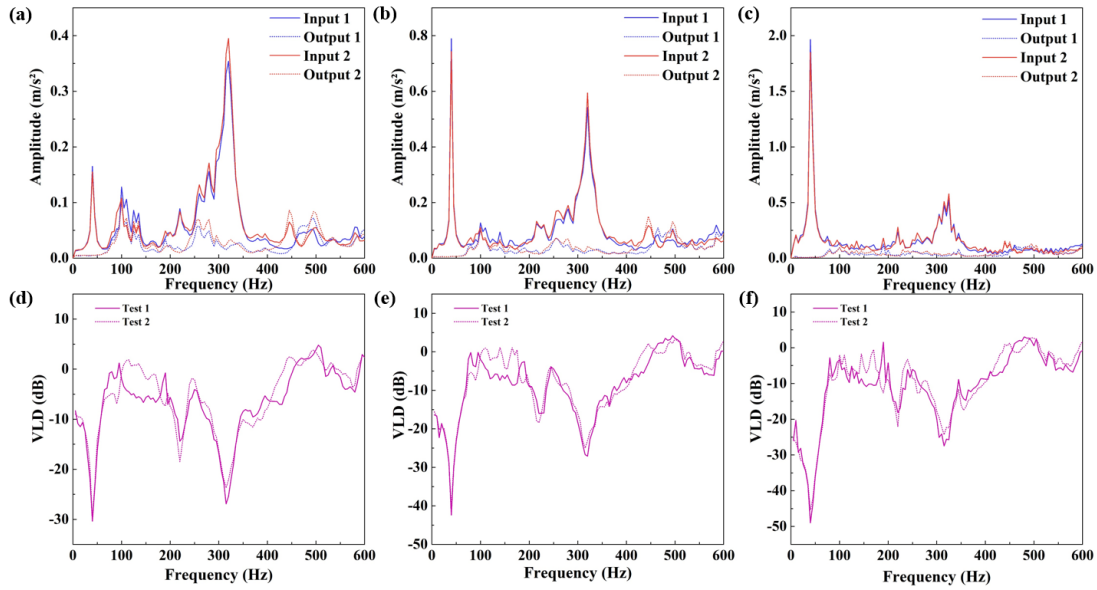


Fig. 20 Vibration response of QILS under the combined effect of rotating transverse excitation and stern longitudinal excitation: (a), (b) and (c) Acceleration input and output responses at speeds of 200rpm, 400rpm and 600 rpm; (d), (e) and (f) VLD at speeds of 200rpm, 400rpm and 600 rpm

Compared with the first two operating conditions, the amplitude magnitude did

not change significantly when the rotational speed was lower under the combined effect of longitudinal and transverse excitation. The trend of the vibration response of the four structures is similar to the response under operating condition ii. The main resonance peaks were not significantly shifted. As the rotational speed increases, the vibration response gradually agrees with the response in the second operating condition. The vibration response under longitudinal excitation is not prominent in the third operating condition and is mainly dominated by the vibration under transverse excitation. This is mainly due to the fact that as the rotational speed increases, the mass block on the balancing disk has a larger moment of inertia and the resulting transverse excitation force gradually takes over. The next reason is that in this test, the longitudinal excitation force applied at the stern is not large considering the safety of the shaft system.

The average vibration response of the two outputs and inputs are averaged to plot the average vibration level difference curves, which are shown in Fig. 21 for both transverse and longitudinal excitation. Under longitudinal and transverse excitation with different rotational speeds, similar to the response under operating condition ii, the solid structure has no vibration isolation effect. Whereas BCC, NILS and QILS produced large vibration isolation band gaps within 100 Hz and in the 200-400 Hz frequency band, it remains that the QILS has a more pronounced vibration isolation effect in the lower frequency band, especially around 40 Hz. Comparing the vibration response under operating condition ii (shown in Fig. 16), there is no significant change in the vibration level difference curve for the third operating condition. At 40 Hz, the maximum amplitude of the level drop at 200 rpm, 400 rpm and 600 rpm are 30.09 dB, 41.44 dB and 47.15 dB, respectively, which are close to the 33.85 dB, 43.16 dB and 47.44 dB of the working condition ii, but the vibration isolation effect is a little bit worse than that of the working condition ii. This is mainly due to the fact that in working condition ii, there is only transverse excitation, while working condition iii is both transverse and longitudinal excitation. In addition, with the increase of rotational speed, the difference of the vibration level difference at 40 Hz decreases compared with the working condition ii, which is 3.76 dB, 1.72 dB and 0.29 dB, respectively. This is mainly due to the fact that the vibration under the longitudinal excitation becomes less and less obvious with the increase of rotational speed in the working condition iii. The vibration of the shaft system is gradually dominated by the vibration under transverse

excitation, and the vibration response gradually converges to the working condition ii.

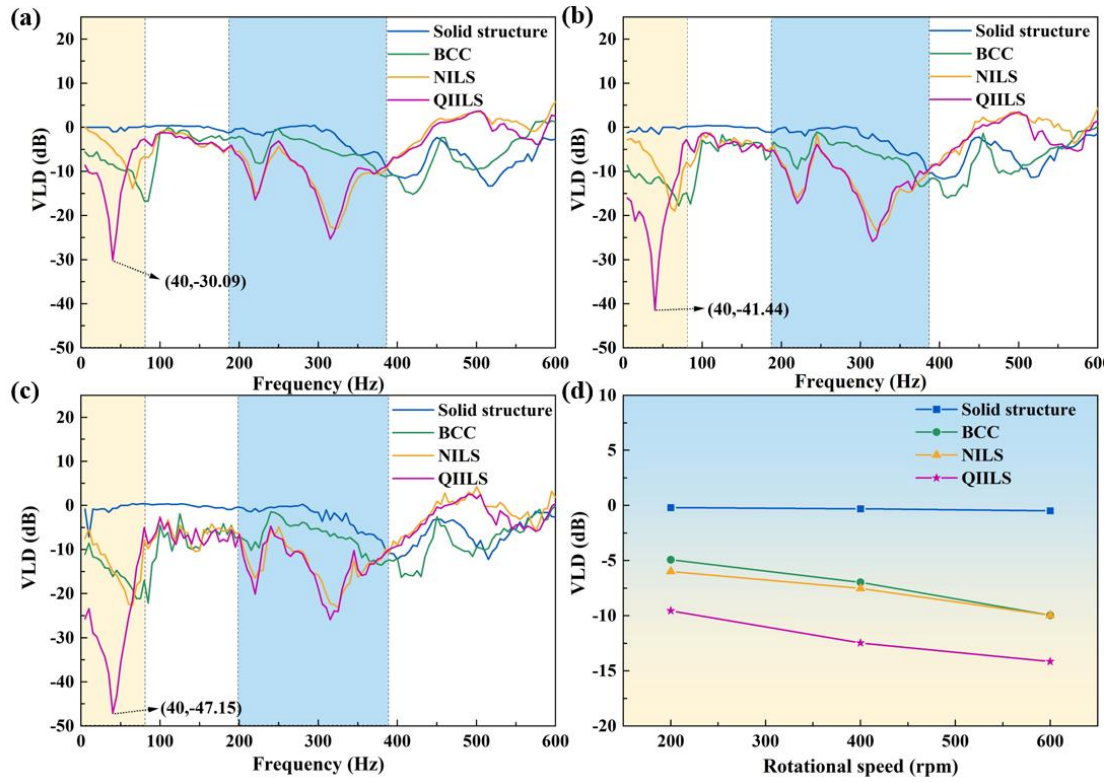


Fig. 21 VLD of different structures under rotating transverse excitation and stern longitudinal excitation: (a), (b) and (c) VLD at 200rpm, 400rpm and 600 rpm; (d) average VLD from 0-300 Hz

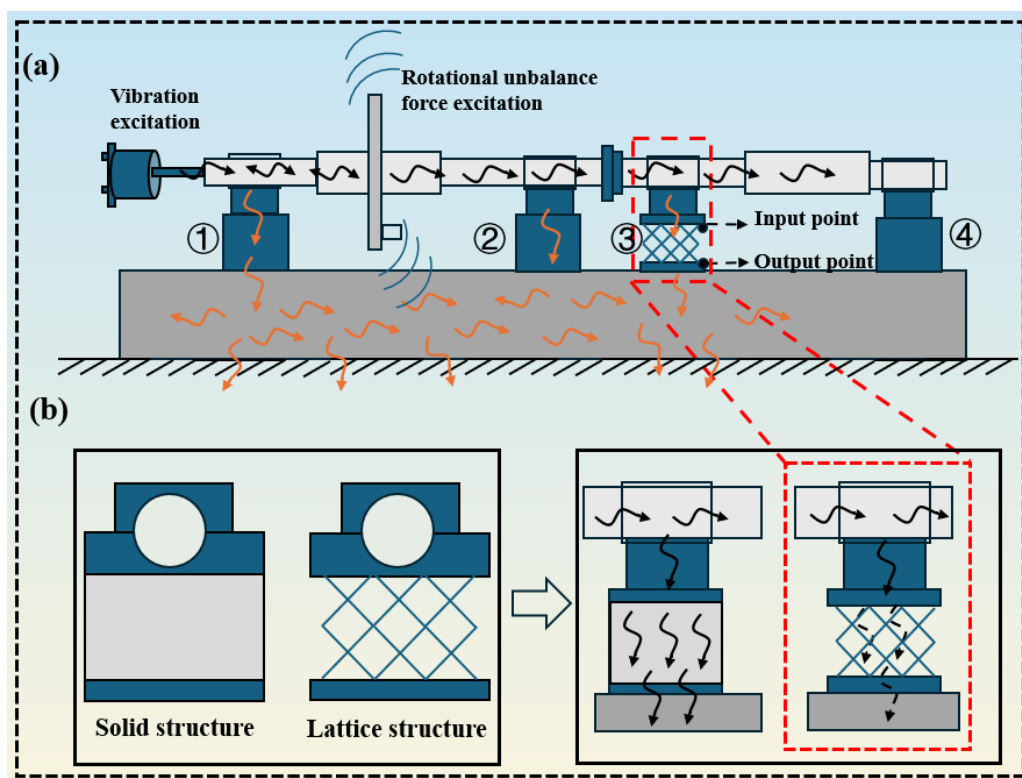


Fig. 22 Schematic diagram of shaft system vibration transmission

In order to analyze in more detail the reason why the vibration isolation becomes better when the rotational speed is increased, Fig. 22 shows a schematic diagram of the transmission of vibrations in the shaft system. 如图 22(a)所示，轴系的艏部受到激励器施加的纵向激励力，且随着轴系转动，平衡盘上的偏心质量块产生不平衡横向激励力。这些振动激励沿着轴系传递，部分振动会通过轴承座①和②以及下方的基座平台传入大地并耗散掉。输入点测得的振动响应为轴的振动响应，输出点测得的振动响应是通过轴系传递到隔振基座③的振动响应。当转速增加时，偏心质量块产生的振动激励逐渐增大，导致输入点的振动响应增大，但与此同时通过轴承座①和②以及基座平台的耗散掉的振动分量也会增大(即轴的振动激励没有完全经过隔振基座③)，从而导致输出点的振动响应会变小。所以转速增大，通过公式(7)计算后的振级落差会增大，即隔振效果变好。

图 22(b)为实心基座与点阵结构隔振基座对比。由于实心基座具有较大的刚性，且对振动没有衰减作用，但是通过 TPMS 点阵结构设计后，中间部分刚性降低，结构的刚性梯度引起的阻抗失配变得更加明显，结构隔振效果越好。其次 IWP 结构比 BCC 点阵结构隔振效果更好主要是 IWP 点阵结构最中间的支杆厚度最小，两侧较厚，当振动从大截面积向小截面积传递时，阻抗增大，能耗

增加，这与 Zhang 等人^[32]的研究结果一致。（还没想好这块怎么进一步改写，先这样，中文方便懂意思）

4. Conclusions

In this paper, BCC, normal TPMS-IWP and multicell interlacing IWP lattice structures with an overall volume fraction of 10% were fabricated using LPBF technology. Uniaxial compression tests as well as shaft system vibration tests are performed to compare with solid structures and to illustrate the effect of different structural types of lattice structures on compression and vibration performance. The main conclusions drawn from this work are:

(1) The compression tests show that the Normal IWP lattice structure (NILS) has better load bearing performance and energy absorption capacity. The mechanical properties of the multicell interlacing structure gradually decrease as the cell of multicell interlacing increases. Due to the multiplication of the number of nodes of the structure, it leads to an earlier stage of densification during compression of the structure.

(2) The vibration response test of the multicell interlacing structures show that with the increase of the cell of multicell interlacing, the structural stiffness and the intrinsic frequency decrease, but the low-frequency vibration isolation performance becomes better, and the vibration isolation bandgap moves to the low frequency. In addition, due to the multicell interlacing design of the structure, it also affects the structural damping ratio and resonance peak.

(3) The vibration isolation test of the shaft system proves that the solid structure has almost no vibration isolation effect. The multicell interlacing design lattice structures have better low-frequency vibration isolation performance than BCC and NILS. The maximum vibration level difference amplitude of the QIILS is close to 50 dB, which demonstrates the effectiveness of the multicell interlacing design for shaft system vibration isolation.

5. References:

- [1] BENEDETTI M, DU PLESSIS A, RITCHIE R O, et al. Architected cellular materials: A review on their mechanical properties towards fatigue-tolerant design and fabrication [J]. *Materials Science and Engineering: R: Reports*, 2021, 144.
- [2] QU D, LIU X, LIU G, et al. Analysis of vibration isolation performance of parallel air spring system for precision equipment transportation [J]. *Measurement and Control*, 2019, 52(3-4): 291-302.
- [3] DALLAGO M, RAGHAVENDRA S, LUCHIN V, et al. The role of node fillet, unit-cell size and strut orientation on the fatigue strength of Ti-6Al-4V lattice materials additively manufactured via laser powder bed fusion [J]. *International Journal of Fatigue*, 2021, 142.
- [4] CLAEYS C, DECKERS E, PLUYMERS B, et al. A lightweight vibro-acoustic metamaterial demonstrator: Numerical and experimental investigation [J]. *Mechanical Systems and Signal Processing*, 2016, 70-71: 853-80.
- [5] SADRNEZHAAD S K, HOSSEINI S A. Fabrication of porous NiTi-shape memory alloy objects by partially hydrided titanium powder for biomedical applications [J]. *Materials & Design*, 2009, 30(10): 4483-7.
- [6] CHU C L, CHUNG C Y, LIN P H. Phase transformation behaviors in porous Ni-rich NiTi shape memory alloy fabricated by combustion synthesis [J]. *Materials Science and Engineering: A*, 2005, 392(1-2): 106-11.
- [7] WU S, LIU X, CHAN Y L, et al. In vitro bioactivity and osteoblast response on chemically modified biomedical porous NiTi synthesized by capsule-free hot isostatic pressing [J]. *Surface and Coatings Technology*, 2008, 202(11): 2458-62.
- [8] CHEN G, CAO P, WEN G, et al. Using an agar-based binder to produce porous NiTi alloys by metal injection moulding [J]. *Intermetallics*, 2013, 37: 92-9.
- [9] ISMAIL M H, GOODALL R, DAVIES H A, et al. Porous NiTi alloy by metal injection moulding/sintering of elemental powders: Effect of sintering temperature [J]. *Materials Letters*, 2012, 70: 142-5.
- [10] ZHU B, LI D, DU C, et al. Near-spherical micron-porous NiTi alloys with high performances fabricated via metal injection molding [J]. *Materials Science and Engineering: A*, 2024, 892: 146114.
- [11] DZOGBEWU T C, DE BEER D. Additive manufacturing of NiTi shape memory alloy and its industrial applications [J]. *Heliyon*, 2023: e23369.
- [12] ASHRAFI M J, AMERINATANZI A, SAEBI Z, et al. Shape memory response of cellular lattice structures: Unit cell finite element prediction [J]. *Mechanics of Materials*, 2018, 125: 26-34.
- [13] NIE Y, REN Y, GAO H, et al. Mechanical Properties of Selective Laser Melting - Processed Multihierarchical Lattice Structure Based on Body - Centered - Cubic Unit Cell [J]. *Advanced Engineering Materials*, 2024.
- [14] SPEIRS M, VAN HOOREWEDER B, VAN HUMBEECK J, et al. Fatigue behaviour of NiTi shape memory alloy scaffolds produced by SLM, a unit cell design comparison [J]. *J Mech Behav Biomed Mater*, 2017, 70: 53-9.
- [15] WEI Y-L, YANG Q-S, LIU X, et al. Multi-bionic mechanical metamaterials: A composite of FCC lattice and bone structures [J]. *International Journal of Mechanical Sciences*, 2022, 213.
- [16] UDDIN M A, BARSOUM I, KUMAR S, et al. Enhancing compressive performance in 3D printed pyramidal lattice structures with geometrically tailored I-shaped struts [J]. *Materials & Design*, 2024, 237.
- [17] YANG L, LI Y, CHEN Y, et al. Topologically optimized lattice structures with superior fatigue performance [J]. *International Journal of Fatigue*, 2022, 165: 107188.
- [18] CORKERY R W, TYRODE E C. On the colour of wing scales in butterflies: iridescence and preferred orientation of single gyroid photonic crystals [J]. *Interface Focus*, 2017, 7(4).
- [19] WINTER B, BUTZ B, DIEKER C, et al. Coexistence of both gyroid chiralities in individual butterfly wing scales of *Callophrys rubi* [J]. *Proc Natl Acad Sci U S A*, 2015, 112(42): 12911-6.
- [20] SEAGO A E, BRADY P, VIGNERON J P, et al. Gold bugs and beyond: a review of iridescence and structural colour mechanisms in beetles (Coleoptera) [J]. *J R Soc Interface*, 2009, 6 Suppl 2(Suppl 2): S165-84.
- [21] CHEN Z, WU B, CHEN X, et al. Energy absorption and impact resistance of hybrid triply periodic minimal surface (TPMS) sheet-based structures [J]. *Materials Today Communications*, 2023, 37:

107352.

- [22] ARAYA M, JASKARI M, RAUTIO T, et al. Assessing the compressive and tensile properties of TPMS-Gyroid and stochastic Ti64 lattice structures: A study on laser powder bed fusion manufacturing for biomedical implants [J]. *Journal of Science: Advanced Materials and Devices*, 2024, 9(1).
- [23] LEHDER E F, ASHCROFT I A, WILDMAN R D, et al. A multiscale optimisation method for bone growth scaffolds based on triply periodic minimal surfaces [J]. *Biomechanics and Modeling in Mechanobiology*, 2021, 20(6): 2085-96.
- [24] JIN J, WU S, YANG L, et al. Ni-Ti multicell interlacing Gyroid lattice structures with ultra-high hyperelastic response fabricated by laser powder bed fusion [J]. *International Journal of Machine Tools and Manufacture*, 2024, 195.
- [25] ZHOU H, ZHANG D Z, HE N. Compressive properties of novel hybrid-dimensional gyroid lattice structure [J]. *Materials Letters*, 2023, 344.
- [26] ZHANG C, ZHENG H, YANG L, et al. Mechanical responses of sheet-based gyroid-type triply periodic minimal surface lattice structures fabricated using selective laser melting [J]. *Materials & Design*, 2022, 214.
- [27] CUTOLO A, BEEVERS E, VAN HOOREWEDER B. A design strategy to enhance the mechanical response of diamond-based lattice structures produced by laser powder bed fusion [J]. *Materials Science and Engineering: A*, 2023, 876.
- [28] BAGHOUS N, BARSOUM I, ABU AL-RUB R K. The effect of Lode parameter on the yield surface of Schoen's IWP triply periodic minimal surface lattice [J]. *Mechanics of Materials*, 2022, 175.
- [29] ZHANG J, SHEN Y, SUN Y, et al. Design and mechanical testing of porous lattice structure with independent adjustment of pore size and porosity for bone implant [J]. *Journal of Materials Research and Technology*, 2022, 18: 3240-55.
- [30] YANG L, LI Y, WU S, et al. Tailorable and predictable mechanical responses of additive manufactured TPMS lattices with graded structures [J]. *Materials Science and Engineering: A*, 2022, 843.
- [31] AL-KETAN O, LEE D-W, ROWSHAN R, et al. Functionally graded and multi-morphology sheet TPMS lattices: Design, manufacturing, and mechanical properties [J]. *Journal of the Mechanical Behavior of Biomedical Materials*, 2020, 102.
- [32] ZHANG C, QIAO H, YANG L, et al. Vibration characteristics of additive manufactured IWP-type TPMS lattice structures [J]. *Composite Structures*, 2024, 327.
- [33] SILVA T, LU J-Y, ABU AL-RUB R K, et al. Investigation on tailoring the width and central frequency of bandgaps of TPMS structures [J]. *International Journal of Mechanics and Materials in Design*, 2023, 20(2): 317-29.
- [34] LU J Y, ALHAMMADI A, GIANNINI V, et al. Elastic Vibration Bandgap of Architected Materials based on Triply Periodic Minimal Surfaces [Z]. 2021 Fifteenth International Congress on Artificial Materials for Novel Wave Phenomena (Metamaterials). 2021: 011-4.10.1109/Metamaterials52332.2021.9577141
- [35] LIN D, ZHANG C, CHEN X, et al. TPMS_Scaffold_Generator: A Scaffold-Structure Generator Based on Triply Periodic Minimal Surfaces [J]. *Additive Manufacturing Frontiers*, 2024, 3(2): 200123.
- [36] STANDARD I. ISO 13314:2011, Mechanical Testing of Metals — Ductility Testing — Compression Test for Porous and Cellular Metals: Ref Number ISO: [S]. 1-7.
- [37] LI S, YANG J-S, YANG F, et al. Fabrication and vibration isolation capacity of multilayer gradient metallic lattice sandwich panels [J]. *Mechanical Systems and Signal Processing*, 2022, 180.